Rheol Acta (2009) 48:97–108
DOI 10.1007/s00397-008-0317-9

ORIGINAL CONTRIBUTION

Flow of branched polymer melts in a lubricated cross-slot channel: a combined computational and experimental study

A. Abedijaberi · J. Soulages · M. Kröger · B. Khomami

Received: 14 February 2008 / Accepted: 1 August 2008 / Published online: 30 October 2008

Abstract Numerical simulations have been performed to evaluate the accuracy of the multimode Giesekus model in predicting the flow behavior of a rheologically well characterized low-density polyethylene melt in a lubricated cross-slot channel. Specifically, the fidelity of the numerical results is established by detailed comparison with flow-induced birefringence measurements in a new optical rheometer with lubricated side walls that allows the creation of ideal two-dimensional flow kinematics that lead to the elimination of end effects commonly encountered in flow birefringence measurements. Based on these comparisons, the ability of the multimode Giesekus model to capture the flow characteristics with reasonable accuracy in the experimentally available Wi range of 21 to 29 has been established. However, it should be noted that the model predictions are, at best, qualitative in the vicinity of the stagnation point. The discrepancy between numerically predicted and experimentally observed stresses in this region is mainly attributed to the inaccuracy of the experimental data that stem from the occurrence of multiple orders of retardation within the measurement volume. Overall, these studies have paved the way for the development of a hi-fidelity lubricated cross-slot channel rheometer.

Keywords Flow modeling · Differential constitutive equation · Rheo-optics · Finite-element analysis · Flow visualization · Polymer melt

A. Abedijaberi · B. Khomami (✉)
Material Research and Innovation Laboratory,
Department of Chemical and Biomolecular Engineering,
University of Tennessee in Knoxville,
Knoxville, TN 37996, USA
e-mail: bkhomami@utk.edu

A. Abedijaberi
e-mail: aabedija@utk.edu

J. Soulages
Hatsopoulos Microfluids Laboratory,
Department of Mechanical Engineering,
Massachusetts Institute of Technology,
Cambridge, MA 02139, USA
e-mail: soulages@mit.edu

M. Kröger
Polymer Physics, Department of Materials, ETH Zürich,
Wolfgang-Pauli-Str. 10, 8093 Zürich, Switzerland
URL: www.complexfluids.ethz.ch

Introduction

The non-Newtonian flow characteristics of polymer melts strongly impact the vast majority of processing operations used to manufacture polymeric products such as mixing, extrusion, fiber spinning, film blowing, or injection molding (Dealy and Wissbrun 1990). Quantitative prediction of velocity and stress distributions in complex flows of polymers is a challenging goal, but offers the promise of more rational process design and optimization. Advances in computational algorithms have largely resolved the long-standing Weissenberg or Deborah number problem that had limited numerical simulations to weakly elastic conditions for many years (Keunings 2001). The steady growth of computational power has made it possible to employ multiple-mode differential or integral constitutive equations that accurately reflect the distribution of relaxation times of real

polymers and to perform time-dependent calculations in complex geometries. To date, stress distributions from flow birefringence measurements together with finite element computational studies in stagnation flows have emerged as an effective test of constitutive model performances in complex flows (Li et al. 1998, 2000; Burghardt et al. 1999; Feigl and Öttinger 1996). In this context, it has become highly relevant to develop constitutive models or mesoscopic descriptions that not only predict the linear and nonlinear flow behavior of polymeric fluids in shear or extension but also are effective in describing nonhomogeneous flows involving mixed shear and extensional deformations.

To this end, constitutive equations derived from kinetic theory (Kröger et al. 2008) and coarse-grained models motivated by atomistic simulation can be expected to guide these efforts. Specifically, during the last decade, several atomistic and course-grained simulation studies (Harmandaris et al. 1998; Kröger and Hess 2000; Likhtman and McLeish 2002; Everaers et al. 2004; Vladkov and Barrat 2006; Foteinopoulou et al. 2006; Tzoumanekas and Theodorou 2006; Kindt and Briels 2007; Kim et al. 2007) have been instrumental in testing the validity of assumptions used in driving constitutive relationships, as well as establishing the relationship between model and molecular parameters.

In recent years, coordinated experimental/computational studies of polymeric systems have typically employed closed-form constitutive equations such as multiple-mode versions of various differential (Giesekus, Phan-Thien–Tanner, Bird–DeAguiar) or integral (Wagner, Papanstasiou–Macosko–Scriven) models (Bird et al. 1987). Such models have had reasonable but not universal success in predicting the mixed kinematics flow of polymer melts and solutions. Specifically, it has been established that the multimode Giesekus model performs exceptionally well in predicting the steady flow kinematics and stress field of moderately concentrated polymeric solutions in complex kinematics flows up to moderate Weissenberg numbers (Li et al. 1998, 2000; Burghardt et al. 1999). In cross-slot geometries, for instance, the Giesekus model has been used by Schoonen et al. (1998) to perform a three-dimensional (3D) analysis of the stagnation flow of a polyisobutylene solution. However, the presence of end effects close to the stagnation point led to experimental birefringence measurements that were three times higher than the numerical predictions. In a flow channel similar to that of Schoonen et al., Peters et al. (1999) studied the performances of the Giesekus model in predicting the complex flow of a polyethylene melt using birefringence isochromatic fringe pattern measurements. Large deviations between the 2D viscoelastic simulations and the experimental results were observed downstream of the stagnation point. This discrepancy was mainly attributed to end effects and beam deflections. In the same cross-slot device, Verbeeten et al. (2002) compared the extended Pom-Pom and Giesekus model predictions with experimental results along the channel symmetry line and observed an over prediction of the maximum stress in the vicinity of the stagnation point due to possible end effects. To date, end effects in flow birefringence experiments have largely prevented a rigorous evaluation of model predictions in complex kinematics flows of polymeric systems. In this study, we evaluate the performances of the multimode Giesekus model in describing the flow behavior of a low-density polyethylene melt (LDPE) melt (studied earlier by Wagner et al. 2000 and Bach et al. 2003) flowing in a lubricated cross-slot channel recently developed by Soulages et al. (2007) that eliminates end effects.

Flow birefringence of polymer melts

Stress distribution measurements using flow birefringence in mixed kinematics flows of polymer melts provide a stringent test of the predictive capabilities of constitutive equations. Flow-induced birefringence is one of the most prevalent noninvasive techniques that allow a complete mapping of stress fields in polymeric systems under flow. In flow birefringence experiments, the direct relationship between the optical and molecular anisotropy expressed by the stress-optical rule is exploited to measure the flow-induced polymeric stresses (Fuller 1995). Birefringence measurements typically involve passing a light beam through a flowing birefringent medium in order to capture the resulting optical anisotropy. Thus, the flow should be 2D in order to ensure the accuracy of the averaged optical properties along the light path. In reality, however, the confining walls of the experimental geometry inevitably lead to end effects. Motivated by experimental evidence that end effects become negligible in channels having an aspect ration greater than 10 (Wales 1976), many researchers have resorted to utilizing large aspect ratio flow channels to minimize the influence of the parasitic shear gradients near the sidewalls. Contrary to this generally accepted view, working with a large aspect ratio is not sufficient to guarantee 2D flows. Recently, systematic studies have conclusively shown that the stress gradients along the beam path near the confining walls cause uncertainties in the effective extinction angle measurement that cannot be eliminated working with large aspect ratios (McHugh et al. 1987; Öttinger

1999). To circumvent the difficulties associated with creating 2D flows, a few researchers have used axisymmetric geometries and compared the integrated optical measurements with numerical simulation predictions to assess the performances of various constitutive models (Li et al. 1998, 2000; Burghardt et al. 1999; Bach et al. 2002). Although the computational demands in such studies are equivalent to those of 2D flows, accurate experimental measurements are very challenging due to parasitic wall effects and/or beam spread. Alternatively, one can perform 3D simulations and compare the integrated stresses along the light path with experimental data. However, the computational burden associated with performing 3D simulations in complex flow geometries with realistic multimode constitutive equations or mesoscopic models is often orders of magnitude higher than 2D simulations and then requires significant super computing resources. In addition, end effects in 3D flows do not allow a reliable measurement of the extinction angle as the small retardance approximation is not valid for polymer melts due to multiple orders of retardation. These difficulties have motivated recent work by Soulages et al. (2007) aimed at developing a novel optical cross-slot channel rheometer whose front and back viewing windows are lubricated so that a controllable complex 2D isothermal flow could be created. Lubricating sidewalls not only eliminates the stress gradients near the walls and, subsequently, the end effects but also makes it possible to use small aspect ratios. This latter property presents the advantage of working with a perfectly collimated beam over the entire channel depth and offers a better control of the temperature in the flow cell.

Problem formulation

Conservation equations

The equations of motion and continuity for an incompressible fluid are given by

$$\mathrm{Re}\left(\frac{\partial \mathbf{u}}{\partial t}+\mathbf{u}\cdot\nabla\mathbf{u}\right)=-\nabla p+\nabla\cdot\boldsymbol{\tau}, \tag{1}$$

$$\nabla\cdot\mathbf{u}=0, \tag{2}$$

where $\mathbf{u}$, p, and $\boldsymbol{\tau}$ represent, respectively, the velocity, the excess pressure, and the deviatoric stress tensor. In what follows, all stresses are nondimensionalized with respect to $\eta_0 V/H$, where η_0 is the polymer zero-shear-rate viscosity, V the average inflow velocity, and H the half channel width (6 mm). In Eq. 1, Re represents the Reynolds number, which is defined as $\mathrm{Re}=\rho VH/\eta_0$ (nearly zero in the parameter range of this study), where ρ denotes the fluid density. The Weissenberg number Wi is defined as $\mathrm{Wi}=\bar{\lambda}V/H$, where $\bar{\lambda}$ represents the polymer mean relaxation time. To complete the set of governing equations, a constitutive model that relates $\boldsymbol{\tau}$ to the velocity field and its gradient is used. The choice of the multimode Giesekus model has been motivated by the success of this model in accurately describing the rheological behavior of concentrated solutions in complex kinematics flows (Li et al. 1998, 2000; Burghardt et al. 1999) and the good description of the rheology of the test fluid in simple shear and uniaxial extension. While the Giesekus model allows to model rheological properties on the macroscale, it does not help to correlate structural properties of the fluid's ingredients with its parameters.

Giesekus model

The Giesekus model (Giesekus 1982) is derived from an elastic dumbbell theory and was originally developed for concentrated polymer solutions and melts. Because of the large polydispersity of the LDPE melt used in this study, a multimode Giesekus model has been used. In this model, the polymeric contribution to the total stress associated with each mode i ($1\leqslant i\leqslant M$) is described by

$$\boldsymbol{\tau}_i+\lambda_i\overset{\nabla}{\boldsymbol{\tau}}_i+\frac{\alpha_i\lambda_i}{\eta_i}(\boldsymbol{\tau}_i\cdot\boldsymbol{\tau}_i)=2\eta_i\dot{\boldsymbol{\gamma}}, \tag{3}$$

and the total polymeric stress in Eq. 1 reads

$$\boldsymbol{\tau}=\sum_{i=1}^{M}\boldsymbol{\tau}_i. \tag{4}$$

The parameter α_i in Eq. 3 is the mobility parameter associated with the anisotropic hydrodynamic drag observed in concentrated solutions and melts ($0\leqslant\alpha_i\leqslant 1$). In this study, The values of α_i are less than 0.5 to ensure monotonic increase of shear stress with shear rate. In Eq. 3, $\overset{\nabla}{\cdot}$, η_i, λ_i, and $\dot{\boldsymbol{\gamma}}$ denote, respectively, the upper convected time derivative, the polymer viscosity, the relaxation time, and the rate of deformation tensor defined as $\dot{\boldsymbol{\gamma}}=\frac{1}{2}[\nabla\mathbf{u}+(\nabla\mathbf{u})^T]$. For each mode, we introduce the dimensionless relaxation time $\Lambda_i=\lambda_i/\bar{\lambda}$ and the dimensionless polymeric viscosity $\beta_i=\eta_i/\eta_0$ so that Eq. 3 can be rewritten in dimensionless form as

$$\boldsymbol{\tau}_i^{\star}+\mathrm{Wi}\,\Lambda_i\tilde{\boldsymbol{\tau}}_i^{\star}+\frac{\alpha_i\,\mathrm{Wi}\,\Lambda_i}{\beta_i}(\boldsymbol{\tau}_i^{\star}\cdot\boldsymbol{\tau}_i^{\star})=2\beta_i\dot{\boldsymbol{\gamma}}^{\star}, \tag{5}$$

where we define $\boldsymbol{\tau}_i^\star = \boldsymbol{\tau}_i/(\eta_0 V/H)$, $\dot{\boldsymbol{\gamma}}^\star = \dot{\boldsymbol{\gamma}}/(V/H)$ and $\tilde{\boldsymbol{\tau}}_i^\star = \overset{\nabla}{\boldsymbol{\tau}}_i/(\eta_0 V^2/H^2)$, introducing the dimensionless time $t^\star = t/(H/V)$.

Computational technique

The numerical technique used in this study is the higher-order- discrete-elastic-viscous-stress (hp-DEVSS) finite element method (Li et al. 1998; Talwar and Khomami 1995). In this technique, a Galerkin discretization is used for the equations of motion and continuity together with a streamline upwind Petrov–Galerkin (SUPG) discretization for the constitutive equation. In the SUPG scheme, the Galerkin weighting function φ is replaced by $\varphi + (\mathbf{u}\cdot\nabla\varphi)h/|\mathbf{u}|$ (Hughes et al. 1989). The hp-DEVSS method also utilizes an additional stabilizing technique to ensure the ellipticity of the momentum equation. Specifically, the polymeric stress is split into its elastic and viscous parts, namely, $\boldsymbol{\tau} = \boldsymbol{\tau}^e + \boldsymbol{\tau}^v$, where $\boldsymbol{\tau}^v = 2\eta\dot{\boldsymbol{\gamma}}$. This reformulation of the momentum equation gives rise to an enhanced ellipticity, which improves convergence. Finally, one can also enhance the momentum equation ellipticity by the addition of the term $\alpha(2\dot{\boldsymbol{\gamma}} - [\nabla\mathbf{u} + (\nabla\mathbf{u})^T])$. Although this term vanishes in the strong form, it is stabilizing in the weak form because of the different basis functions used for the discretization of $\mathbf{u}$ and $\dot{\boldsymbol{\gamma}}$ (Rajagopalan et al. 1990).

In the Galerkin method, the same basis functions are used for both the trial and test functions. In the hp-DEVSS technique, these basis functions are defined as linear combinations of Legendre polynomials (Talwar et al. 1994). Within each element, the dependent variables are approximated as

$$\boldsymbol{u} = \sum_{i=1}^{N_u} \boldsymbol{u}^i N_i, \quad p = \sum_{i=1}^{N_p} p^i N_i,$$
$$\boldsymbol{\tau} = \sum_{i=1}^{N_\tau} \boldsymbol{T}^i N_i, \quad \dot{\boldsymbol{\gamma}} = \sum_{i=1}^{N_{\dot{\gamma}}} \dot{\boldsymbol{\gamma}}^i N_i, \tag{6}$$

where $\boldsymbol{u}^i$, p^i, $\boldsymbol{T}^i$, and $\dot{\boldsymbol{\gamma}}^i$ constitute the set of unknown expansion coefficients for $\boldsymbol{u}$, p, $\boldsymbol{\tau}$, and $\dot{\boldsymbol{\gamma}}$, respectively. In Eq. 6, N_i are the basis functions and N_u, N_p, N_τ, and $N_{\dot{\gamma}}$ determine the order of polynomials to approximate $\boldsymbol{u}$, p, $\boldsymbol{\tau}$, and $\dot{\boldsymbol{\gamma}}$. The choice of respective polynomial orders must satisfy the Berzzi–Babuska condition, i.e., $N_p = 1$ as $N_u = 2$ in our study. Earlier studies (Guenette 1995; Grillet et al. 1999) have shown that the optimum set of polynomial orders for the other variables is then $N_\tau = N_{\dot{\gamma}} = 1$. In the other words, $\boldsymbol{u}$ is discretized using biquadratic basis functions and $\boldsymbol{\tau}$, p, and $\dot{\boldsymbol{\gamma}}$ are approximated by bilinear functions.

Both slip and symmetry boundary conditions have been used. In particular, we introduce a slip velocity u_{slip} so that the velocities on the sidewalls obey $\mathbf{u}\cdot\mathbf{t} = u_{\text{slip}}$ and $\mathbf{u}\cdot\mathbf{n} = 0$, where $\mathbf{t}$ and $\mathbf{n}$ represent unit vectors, respectively, tangent and normal to the boundary walls in the laboratory frame defined in Fig. 1. In addition, the in- and outflow channel centerline velocities together with the τ_{xy} component of the stress tensor are set to zero due to symmetry. At the channel inlet, the velocity profile ($u_y = u_y(x)$ and $u_x = 0$) and the necessary components of the stress tensor are specified by assuming a fully developed flow. At the exit, a fully developed velocity profile ($u_x = u_x(y)$ and $u_y = 0$) is also specified. For most nonlinear constitutive equations, such as the Giesekus model, analytical solutions are not available even under fully developed conditions. Thus, the fully developed inlet and outlet boundary conditions were generated numerically in a mesh with the same number of nodes and node locations as the mesh used in the inflow and outflow channels of the flow computations.

Due to the inherent symmetry of the flow channel, the computational domain is restricted to one quarter of the flow domain, as shown in Fig. 1. In order to check the accuracy of the calculations, we have selected three structured meshes based on the same topology as illustrated in Fig. 2. The mesh with the lowest discretization in Fig. 2a was chosen to ensure convergence of the solution in the fully developed region of the inlet and outlet channels. In all meshes, the nodes were pushed towards the walls in order to capture the sharp velocity and stress gradients in these regions. In addition, nodes were positioned to guarantee a satisfactory discretization near the stagnation point while avoiding drastic size differences between nearby elements. The finer meshes in Fig. 2b, c were designed to provide

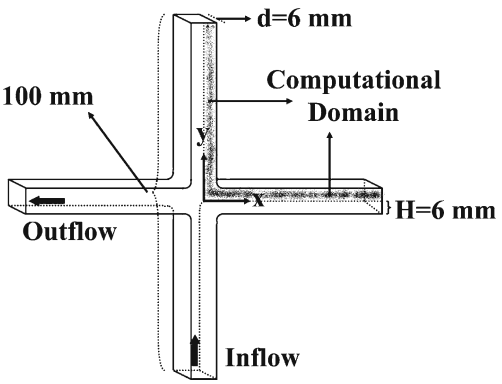

Fig. 1 Schematic view of the computational domain

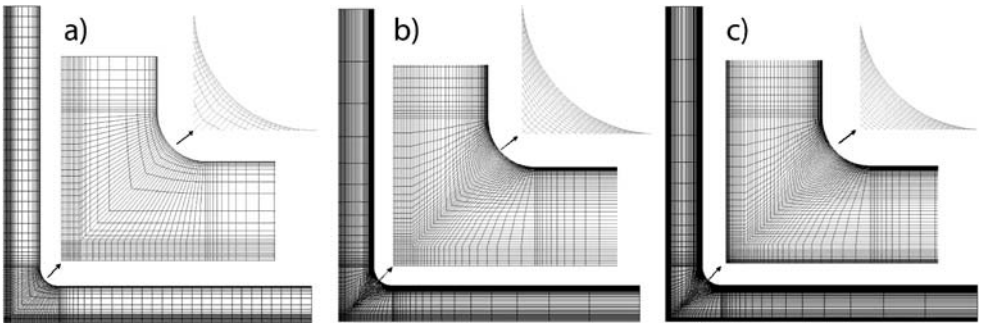

Fig. 2 Finite element meshes with **a** 3,492, **b** 4,500, and **c** 6,400 elements

refinements in the regions where oscillations in stresses were observed at lower discretization levels.

The full system of discretized equations is solved using a frontal solver Newton–Raphson iteration method. Details of this method can be found in Talwar and Khomami (1992). In the Newton–Raphson method, convergence is ensured if the initial guess is sufficiently close to the exact solution. To ensure a good initial guess, we have used the Weissenberg number Wi as the continuation parameter in our calculation. To do so, Wi was first set to zero and the linear Newtonian flow problem was solved. Next, the solution of this calculation was used as a guess for the next Wi number. Increments of 0.01 to 0.25 were used to capture the solution up to Wi equals 29. The convergence criterion used in the Newton–Raphson scheme is $\sum_{i=1}^{e} \Delta a_i^2 \leq 10^{-6}$, where $\Delta a_i^2 = (a_i^{k+1} - a_i^k)^2$ and a_i^k represent the value of the unknown expansion coefficients $\boldsymbol{u}^i$, p^i, $\boldsymbol{T}^i$, and $\dot{\boldsymbol{\gamma}}^i$ at the kth iteration.

Experiment

Experimental methods

A complete description of the flow geometry and lubrication technique can be found in Soulages et al. (2007). The experimental geometry is shown in Fig. 3. The channel consists of four transparent arms of length 50 mm, which are made visible using flush-mounted glass viewing windows (Schott SF-57, 8 mm thickness). The width and height of the flow cell equal 12 and 6 mm, so that its aspect ratio is 0.5. In the vicinity of the stagnation point, rounded corners with a radius of 3 mm ensure a smooth transition between the channel in- and outlets. At each arm entrance, a set of two opposite oil slits delivers the lubricant (silicone oil) at a constant volumetric flow rate. The lubricant flow rate can be optimized at any time during an experiment using birefringence and particle tracking velocimetry measurements, and the oil pressure is monitored so that planar conditions can effectively be reached. The lubricant is dragged along the glass windows by the incoming polymer streams, resulting in an oil film whose thickness is of the order of several microns. The two opposed polymer melts impinge in the middle of the flow cell and exit the channel through its two horizontal arms. The entire channel is fixed to a computer-controlled XY-translation stage so that flow birefringence can be measured in the channel transparent section.

In our study, the stress field is obtained from pointwise flow-induced birefringence measurements (Fuller 1995). The optical train is visible in Fig. 3 and is identical to Galante (1991). This technique is based on a polarization modulation method, which is thoroughly described in Soulages (2007). It allows a direct measurement of the retardation δ and extinction angle χ of the birefringent polymer melt within the laser beam diameter of 120 μm. The dc component (I_{dc}) of the modulated light intensity collected at the detector is measured by means of a low pass filter. The first and second Fourier components (I_ω and $I_{2\omega}$) are sampled

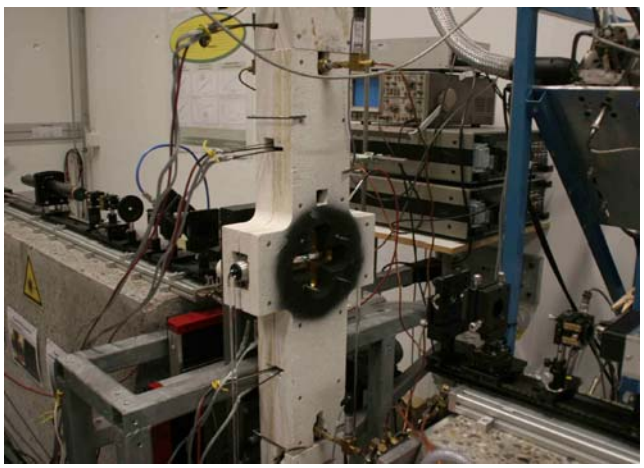

Fig. 3 Experimental setup: the cross-slot flow channel is attached to an XY-translation stage whereas the flow-induced birefringence optical elements are mounted on a fixed stone support plate

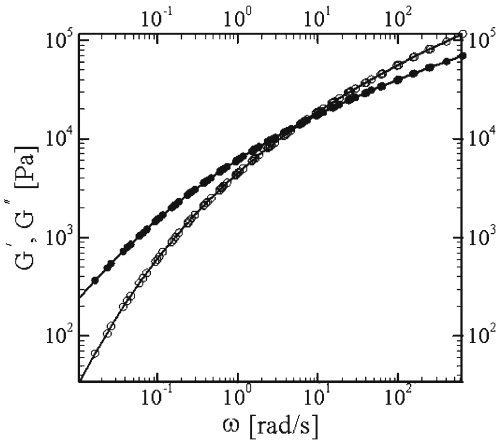

Fig. 4 Storage (*open symbols*) and loss (*full symbols*) moduli at 170 °C together with the calculated spectrum predictions (*full lines*)

using two lock-in amplifiers. After the experimental determination of the calibration constants (J_1 and J_2), the ratios of the Fourier components to the dc intensity make it possible to define optical signals that directly relate the optical properties to the sample retardation δ and extinction angle χ, i.e.,

$$R_\omega = -\frac{I_\omega}{2J_1 I_{\mathrm{dc}}} = \sin(\delta)\cos(2\chi),$$
$$R_{2\omega} = \frac{I_{2\omega}}{2J_2 I_{\mathrm{dc}}} = \sin^2\left(\frac{\delta}{2}\right)\sin(4\chi). \qquad (7)$$

Equation 7 only involves trigonometric functions of χ and δ. In practice, polymer melts show very large levels of birefringence with retardations δ often exceeding 2π. Except in the fully developed region, we could not accurately determine the number of multiples of 2π. That is why we have restricted our comparisons to the optical data of Eq. 7 in which χ and δ could be numerically computed from the simulated stress tensor using the stress-optical rule, i.e.,

$$\chi = \frac{1}{2}\tan^{-1}\left(\frac{2\tau_{xy}}{\tau_{xx}-\tau_{yy}}\right), \qquad \delta = \frac{4\pi dC}{\lambda}\frac{\tau_{xy}}{\sin(2\chi)}, \qquad (8)$$

where the x axis is aligned along the flow direction in Fig. 1, λ is the wavelength of the light beam, d is the channel thickness, and C is the stress-optical coefficient. This coefficient was set to $C = 1.7 \times 10^{-9}$ Pa^{-1}, as determined in Soulages (2007). For polymer melts, the validity of the stress-optical rule has extensively been shown in shear flows (Janeschitz-Kriegl 1983; Wales 1976; Rajagopalan et al. 1992). Recently, the validity of the stress-optical rule has also been confirmed in uniaxial elongational flows, for applied stresses not exceeding 1 MPa (Venerus et al. 1999; Luap et al. 2005, 2006). Beyond this value, the failure of the rule is often associated to the chain finite extensibility (Kröger 2004), but the critical stress levels are generally not accessible in practice (Kröger et al. 1997).

The velocity field in the fully developed inflow region of the flow cell is obtained from particle tracking velocimetry measurements to allow determination of the slip velocity at the channel lateral walls in Section "Determination of the slip velocity". Tracer particles mixed with the polymer melt are illuminated from the front so that the marker displacements can be tracked as a function of time and imaged onto a CCD camera (Soulages 2007).

Test fluid rheological characterization

Our test fluid is a commercial-grade, low-density polyethylene (LDPE 1810H from Basell) fully characterized in both shear and extension. An 11-mode Giesekus model has been used to describe the fluid rheology as it provides a good fit to the rheological measurements. The linear parameters for each mode η_i and λ_i are determined based on the linear viscoelastic response. The linear viscoelasticity has been measured at 170 °C in cone-and-plate geometry (50 mm, 4 °) using a stress-controlled shear rheometer (Paar Physica, model UDS 200). The relaxation spectra shown by solid lines in Fig. 4 were calculated using the Iris program (Winter and Mours 1990–2004). The method of spectra calculation can be found elsewhere (Baumgärtel and Winter 1989). The discrete relaxation time spectrum is given in Table 1. The nonlinear parameters α_i are obtained by fitting the model predictions to the steady shear data, namely, the shear viscosity and the first normal stress difference as illustrated in Fig. 5, and to the uniaxial extensional viscosity data shown in Fig. 6. The steady shear data in Fig. 5 were measured at 170 °C in cone-and-plate geometry (50 mm, 8.5 °) using a mechanical

Table 1 Giesekus parameters: η_i, λ_i, obtained from linear viscoelasticity data and α_i from steady shear and transient uniaxial extensional data

Mode (i)	1	2	3	4	5	6	7	8	9	10	11
η_i (Pa s)	60.900	62.213	159.691	496.439	711.020	1,333.339	2,462.8	3,471.9	5,545.3	3,310.3	5,111.1
λ_i (s)	0.0005	0.0016	0.0051	0.0166	0.0534	0.1718	0.5522	1.7750	5.7080	18.3500	59.0000
α_i	0.3	0.3	0.3	0.3	0.3	0.3	0.3	0.3	0.25	0.2	0.05

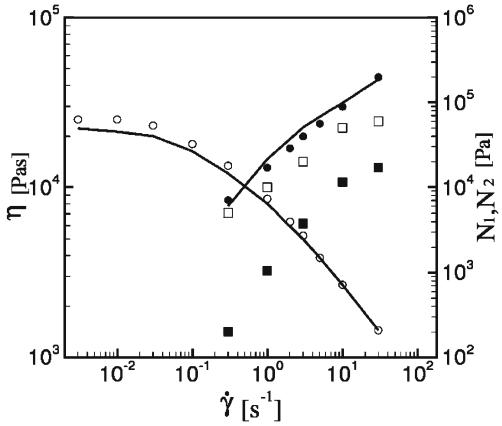

Fig. 5 Steady shear viscosity (*open circle symbols*) and first (*full circle symbols*) and second (*full square symbols*) normal stress difference at 170 °C together with the Giesekus model predictions (*open square symbols* for the second normal stress difference and *full lines* for the shear viscosity and the first normal stress difference)

spectrometer (Rheometric Scientific, model RMS 800) equipped with a force rebalance transducer and in-house electrically heated tools (Meissner et al. 1989). For the second normal stress difference measurements, a cone-partitioned plate geometry was used. A detailed description of this technique can be found in Pollett (1995), Meissner et al. (1989), and Schweizer (2002, 2003). The uniaxial extensional viscosity data in Fig. 6 were collected at 170 °C using a RME rheometer (Meissner and Hostettler 1994; Schweizer 2000) for Hencky strain rates ranging from 0.01 to 1 s^{-1}. The Giesekus model parameters were obtained by minimizing the weighted least squares of the deviations of the model predictions from the experimental measurements. The resulting model parameters are summarized in Table 1. The polymer mean relaxation time $\bar{\lambda}$ was measured from creep tests at 170 °C performed in a cone-and-plate geometry (30 mm, 4°) at a constant shear stress of $\tau_0 = 8$ Pa using a stress-controlled rotational shear rheometer (Anton Paar - Physica, model MCR 300). The mean relaxation time equals $\bar{\lambda} = 16.5$ s.

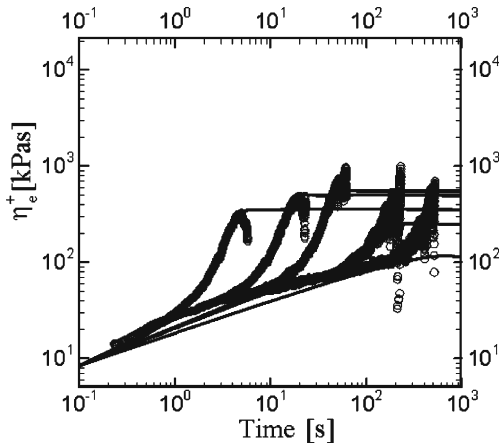

Fig. 6 Uniaxial extensional viscosity (*open symbols*) measured at 170 °C together with the Giesekus model predictions (*full lines*). Hencky strain rate range: 0.88, 0.25, 0.1, 0.028, and 0.00971 s^{-1}

Results

Determination of the slip velocity

The computational results with no-slip boundary conditions at the channel lateral walls did not compare favorably with the experimental results even in the fully developed region, as shown in Fig. 7a. Upon further examination of the experimental cross-slot flow, it was determined that some of the lubricant used to coat the transparent windows of the flow cell had migrated towards the brass solid walls, giving rise to a fully developed encapsulated flow. Hence, all solid surfaces in the experimental setup are lubricated with a very thin lubricant layer of the order of several microns. Therefore, we had to incorporate this effect into our computations in order to better capture the experimental flow conditions. The simplest way to do so was to introduce a slip velocity u_{slip} at the channel sidewalls.

In the fully developed region of the flow cell, the polymer kinematics were derived from particle tracking velocimetry measurements. However, it was especially difficult to obtain reliable results close to the channel solid boundaries because of parasitic light reflections at the brass sidewalls making the marker recognition difficult. Hence, the slip velocity could not be experimentally determined at the channel lateral walls. Therefore, we have numerically simulated results for different slip velocities in order to determine their optimum value for each Weissenberg number.

The optimum slip velocity was obtained via a regression analysis by minimizing the overall differences between the computed and measured velocity (Fig. 7a) and stress fields (Fig. 7b, c) in the channel fully developed region. Following this procedure, the best agreement was found for slip velocities of 5.6 and 6.1 mm/s at Wi = 21 and 29, respectively. It should be noted that the assumption of a uniform slip velocity in the fully developed region is quite reasonable, as the thickness of the lubricant layer is expected to remain nearly constant. However, one would expect variations in the lubricant thickness around the rounded corners next to the stagnation region. Since the lubricant reflections prevent us from measuring a reliable slip velocity at

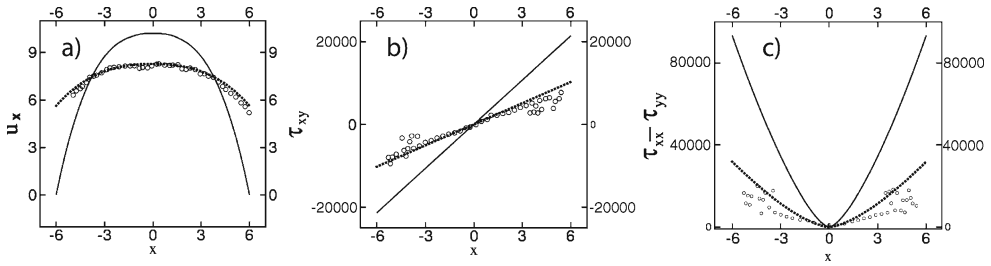

Fig. 7 **a** Velocity profile, **b** shear stress profile, and **c** normal stress profile at Wi = 21 in the channel fully developed inflow region: experimental data (*open circles*) and computational results using no-slip (*solid line*) and slip (*dotted line*) boundary conditions with a slip velocity of $u_{slip} = 5.6$ mm/s

the channel lateral walls, we have used a constant slip velocity all along the sidewalls. As a regression technique has been used to obtain the optimum slip velocity u_{slip}, it is highly relevant to assess the influence of small changes in the slip velocity on the predicted stress and velocity profiles. Figure 8a–c shows the different velocity and stress profiles for variations in the slip velocity of 0.1%, 0.5%, 1%, and 5% at a Weissenberg number of Wi = 21. It can clearly be seen that differences in the velocity and stress profiles in the fully developed region of the flow cell become visible for variations in the slip velocity of the order of 0.5%.

Results at Wi = 21

In order to evaluate the fidelity of the Giesekus model in modeling the mixed kinematics flow of our test fluid, we have focused our data analysis on various locations in the inflow ($y/H = 0.2$, 1.5, and 5) and outflow ($x/H = 0.2$, 1.5, and 5) channels as represented by the cross-slot schematic view in Figs. 9 and 10. These locations have been chosen to assess the ability of the Giesekus model to capture the flow behavior in simple shear, mixed kinematics, and planar extension. Figure 9a shows the experimental and computational optical results in the inflow channel arm. Because of the lubricant light reflections leading to unreliable experimental optical results at the channel edges, the data presented in Figs. 9 and 10 are restricted to the range $-0.6 \leqslant x/H \leqslant 0.6$ and $-0.6 \leqslant y/H \leqslant 0.6$.

At $y/H = 5$ (open triangle symbols), the model provides a good prediction of both the R_ω and $R_{2\omega}$ optical signals. This agreement is expected as the slip velocity has been chosen by matching the stress and velocity profiles in this region of the flow cell. The slight differences observed between the predicted and experimental values are due to the fact that the slip velocity was obtained by minimizing the overall deviations between the measured and computed velocity and stress fields. At $y/H = 1.5$ (filled square symbols), a good agreement is also found between the optical and model data. Thus, in the mixed kinematics region, where the polymer melt extensional thickening is not very pronounced, the Giesekus model is successful in predicting the flow dynamics. However, in the region of planar extensional flow at $y/H = 0.2$ (open circle symbols), the model predictions, although reasonable, are not quantitative. Specifically, the magnitude of oscillations in R_ω close to the stagnation point that result from rapid change of stresses and the corresponding order change of the retardation angle is not captured accurately by the simulations. Moreover, the $R_{2\omega}$ optical signal is underpredicted. However, it should be noted that the quality of the experimental data in this region of the channel is not very good. In particular, oil film reflections together with multiple orders of retardation occurring within the cross section of the laser beam

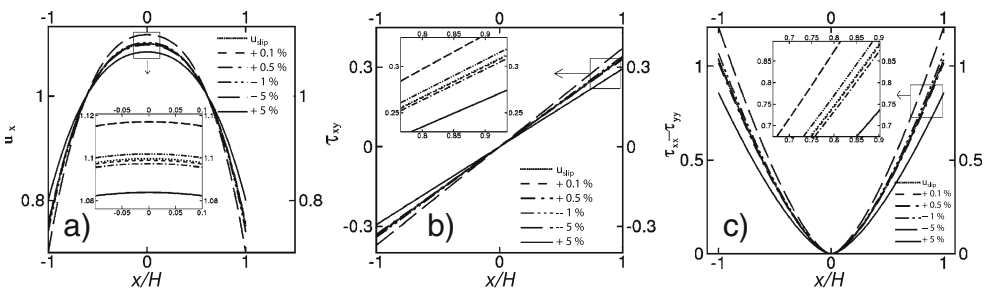

Fig. 8 Kinematics and stress variations caused by minor changes in the optimum slip velocity, i.e., $u_{slip} = 5.6$ mm/s. **a** Velocity profile, **b** shear stress profile, and **c** normal stress profile in the fully developed region at Wi = 21

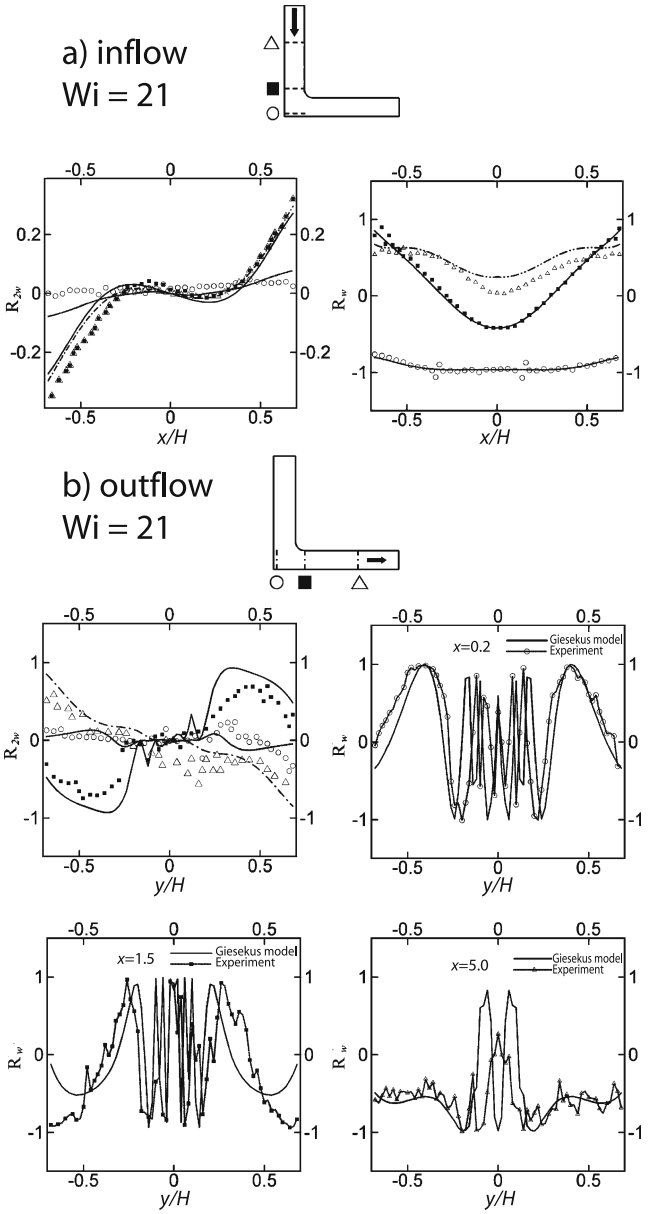

Fig. 9 Comparison between the experimental birefringence data and the viscoelastic flow simulation for R_w and R_{2w} using the Giesekus model in the **a** inflow and **b** outflow channels at Wi = 21 (wall shear rate at the channel entrance = 2.4 unit; extension rate at the stagnation point = 1.2 unit). Data presented at x/H or $y/H = 0.2$ (*circles*), 1.5 (*squares*) and 5 (*triangles*)

make the experimental results questionable. In the outflow channel (see Fig. 9b), although the simulations are successful in qualitatively predicting the flow behavior at $x/H = 0.2$, the predictions along the channel centerline are not very accurate. This underlines the fact that the stress relaxation is not qualitatively captured by the simulations. Moreover, the $R_{2\omega}$ predictions in the outflow channel are qualitative at best.

Results at Wi = 29

Figure 10a, b depicts the experimentally measured and computed optical signal distribution at a Weissenberg number of Wi = 29 in the inflow and outflow channels, respectively. The quality of the predictions in the inflow channel is very similar to those obtained at Wi = 21, except for $y/H = 0.2$. At this location, the model predictions are not as accurate as their Wi = 21 counterpart. Although the experimental $R_{2\omega}$ optical signal is qualitatively captured by the model, large discrepancies are

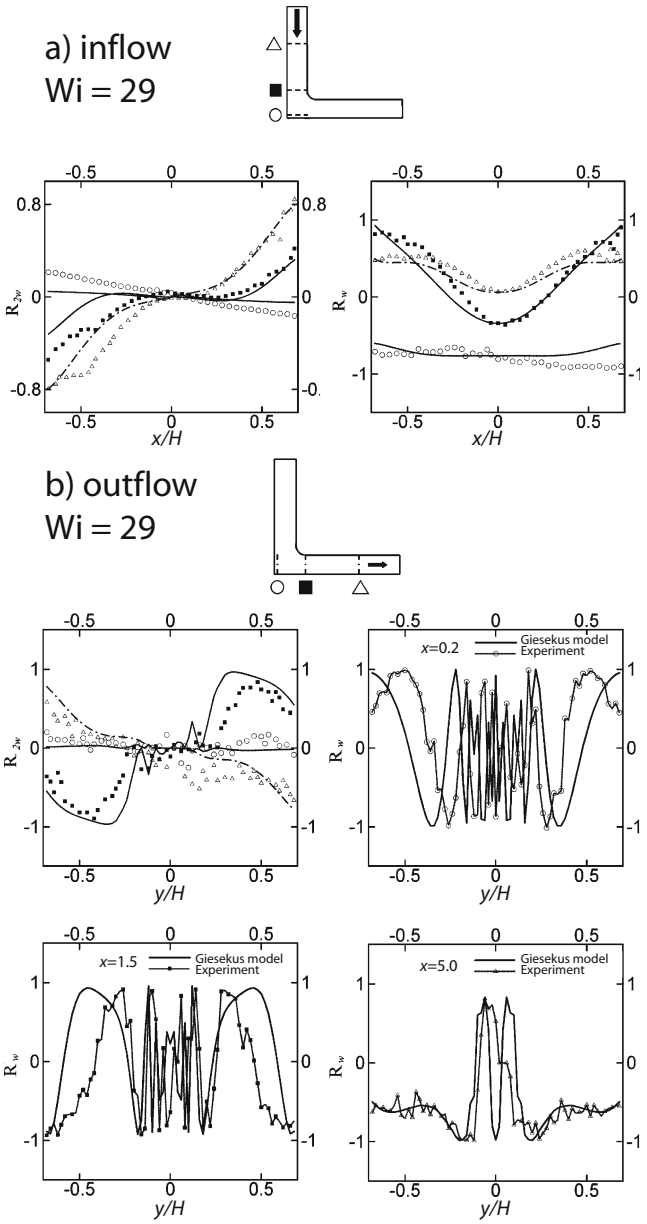

Fig. 10 Same as Fig. 9 for Wi = 29 (wall shear rate at the channel entrance = 3.3 unit; extension rate at the stagnation point = 1.7 unit)

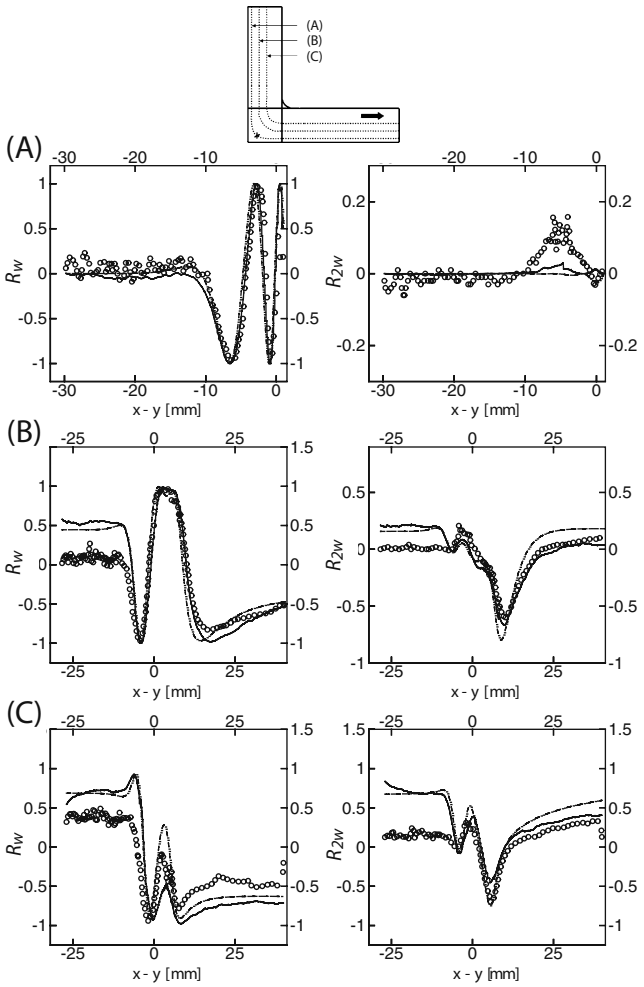

Fig. 11 Comparison between optical properties (R_w and R_{2w}) that were measured experimentally (*circles*), calculated by Lagrangian streamline integration based on measured kinematics (*solid line*), and determined with self-consistent simulations (*dash-dot-dotted line*). The data are presented along streamlines *A*, *B*, and *C* at Wi = 21

observed for the R_ω optical data. The Giesekus model deficiency in predicting the experimental data at this Wi number becomes even more evident in the outflow channel. In Fig. 10b, the experimental data predictions are poor at $x/H = 0.2$. In particular, the number of peaks in the measured optical signals is not accurately predicted by the Giesekus model. This discrepancy is not observed at $x/H = 1.5$, where the number of peaks is the same as the experimental data. The R_ω predictions at $x/H = 5$ are similar to those at Wi = 21. It should be mentioned that the effect of multiple retardation orders at length scale of the beam diameter becomes even more visible at this Weissenberg number, where a significant stress boundary layer is formed near the stagnation point. That is why the averaged optical properties measured using the existing experimental setup are questionable. Therefore, the disagreement observed between the measured and computed quantities at Wi = 29 cannot be solely attributed to the inadequacy of the Giesekus model.

Analysis along selected streamlines

To shed additional light on the source of the discrepancy between the experimentally measured optical properties and those of self-consistent numerical simulations, we have performed Lagrangian integration based on measured kinematics to determine the stress and, in turn, the optical properties along selected streamlines. Overall, there is relatively good agreement between the self-consistent simulation results and the Lagrangian computations. However, it should be noted that, near the stagnation point and in the extensionally dominated flow regime, the self-consistent simulations provide a better description of the experimental data (see Figs. 11 and 12). This comparison further

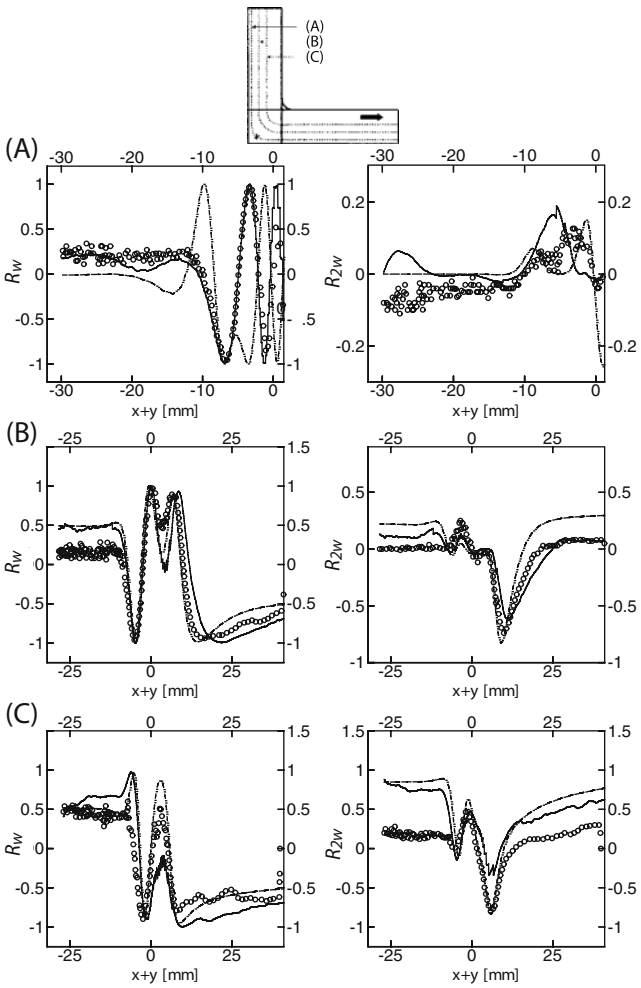

Fig. 12 Same as Fig. 11 for Wi = 29

underlines the fact that the discrepancy between the computational result and experimental findings in the extensionally dominated flow regime can be mainly attributed to the inaccuracy of the experimental data in this regime. Specifically, the stresses and optical properties cannot be measured accurately due to multiple order effects on the length scale of the beam diameter, and accurate kinematics measurements are not possible due to significant light reflection from the lubricant oil.

Conclusion

Numerical simulations of a well-characterized, branched, low-density polyethylene melt in a lubricated cross-slot channel geometry have been performed for a range of Weissenberg numbers. Due to the fact that all the side walls of the cross-clot rheometer are lubricated, comparison of the experimental flow birefringence measurements had to be made with self-consistent 2D flow simulation with an optimum slip velocity. Based on these comparisons, it can be concluded that the Giesekus model can accurately predict the flow characteristics at $\mathrm{Wi} = 21$. However, the model predictions $\mathrm{Wi} = 29$ remain qualitative at best. The discrepancy between the numerically predicted and experimentally measured optical properties cannot be solely attributed to the inadequacy of the constitutive model, as the current experimental protocol is ineffective near the stagnation point, as well as along the plane of symmetry in the outlet channel. The limitation of the current experimental technique stems from multiple orders of retardation within the cross section of the laser beam and oil film reflections occurring close to the stagnation point. Overall, this study has clearly demonstrated the potential of this approach to accurately determine the kinematics and stresses in a 2D flow geometry that can be used to evaluate the fidelity of constitutive equations or mesoscopic models of polymer dynamics in mixed kinematic flows. To make this promise a reality, improvements in the experimental method are required. These would involve a new oil delivery design together with a reduction of the laser beam dimensions, as well as more advanced data analysis strategies.

Acknowledgements B.K. acknowledges financial support from NSF (CBET-0651497). J.S. thanks Thomas Schweizer, Jürg Hostettler and Fredy Mettler for their valuable assistance in performing the experiments.

References

Bach A, Rasmussen HK, Longin PY, Hassager O (2002) Growth of non-axisymmetric disturbances of the free surface in the filament stretching rheometer: experiments and simulation. J Non-Newton Fluid Mech 108:163–186

Bach A, Rasmussen HK, Hassager O (2003) Extensional viscosity for polymer melts measured in the filament stretching rheometer. J Rheol 47:429–441

Baumgärtel M, Winter HH (1989) Determination of discrete relaxation and retardation time spectra from dynamic mechanical data. Rheol Acta 28:511–519

Bird RB, Curtiss CF, Armstrong RC, Hassager O (1987) Dynamics of polymeric liquids, vol 2, kinetic theory. Wiley, New York

Burghardt WR, Li JM, Khomami B, Yang B (1999) Uniaxial extensional characterization of a shear thinning fluid using axisymmetric flow birefringence. J Rheol 43:147–165

Dealy JM, Wissbrun KF (1990) Melt rheology and its role in plastics processing. Theory and applications. Van Nostrand Reinhold, New York

Everaers R, Sukumaran SK, Grest GS, Svaneborg C, Sivasubramanian A, Kremer K (2004) Rheology and microscopic topology of entangled polymeric liquids. Science 303:823

Feigl K, Öttinger HC (1996) A numerical study of the flow of a low-density-polyethylene melt in a planar contraction and comparison to experiments. J Rheol 40:21–35

Foteinopoulou K, Karayiannis NC, Mavrantzas VG, Kröger M (2006) Primitive path identification and entanglement statistics in polymer melts: results from direct topological analysis on atomistic polyethylene models. Macromolecules 39:4207

Fuller GG (1995) Optical rheometry of complex fluids. Oxford University Press, Oxford

Galante SR (1991) An investigation of planar entry flow using a high-resolution flow birefringence method. PhD thesis, Carnegie-Mellon University

Giesekus H (1982) A simple constitutive equation for polymer fluids based on the concept of deformation-dependent tensorial mobility. J Non-Newton Fluid Mech 11:69–109

Grillet AM, Yang B, Khomami B, Shaqfeh ESG (1999) Modeling of viscoelastic lid driven cavity flow using finite element simulations. J Non-Newton Fluid Mech 88:99–131

Guenette R (1995) A new mixed finite element method for computing viscoelastic flows. J Non-Newton Fluid Mech 60:27

Harmandaris VA, Mavrantzas VG, Theodorou DN (1998) Atomistic molecular dynamics simulation of polydisperse linear polyethylene melts. Macromolecules 31:7934

Hughes TJR, Franka LP, Hulbert GM (1989) A new finite element formulation for computational fluid dynamics: viii. the galerkin/least-squares method for advective-diffusive equations. Comput Methods Appl Mech Eng 73:173–189

Janeschitz-Kriegl H (1983) Polymer melt rheology and flow birefringence, from the series polymers, properties and applications. Springer, Berlin

Keunings R (2001) Advances in the computer modeling of the flow of polymeric liquids. Comput Fluid Dyn J 9: 449–458

Kim JM, Keffer DJ, Kröger M, Edwards BJ (2007) Rheological and entanglement characteristics of linear chain polyethylene liquids in planar Couette and planar elongational flows. J Non-Newton Fluid Mech 152:168–183

Kindt P, Briels WJ (2007) A single particle model to simulate the dynamics of entangled polymer melts. J Chem Phys 127:134901

Kröger M (2004) Simple models for complex nonequilibrium fluids. Phys Rep 390:453–551

Kröger M, Hess S (2000) Rheological evidence for a dynamical crossover in polymer melts via nonequilibrium molecular dynamics. Phys Rev Lett 85:1128

Kröger M, Luap C, Muller R (1997) Polymer melts under uniaxial elongational flow: stress-optical behavior from experiments and NEMD computer simulations. Macromolecules 30: 526–539

Kröger M, Ammar A, Chinesta F (2008) Consistent closure schemes for statistical models of anisotropic fluids. J Non-Newton Fluid Mech 149:40–55

Li JM, Burghardt WR, Yang B, Khomami B (1998) Flow birefringence and computational studies of a shear thinning polymer solution in axisymmetric stagnation flow. J Non-Newton Fluid Mech 74:151–193

Li JM, Burghardt WR, Yang B, Khomami B (2000) Birefringence and computational studies of a polystyrene Boger fluid in axisymmetric stagnation flow. J Non-Newton Fluid Mech 91:189–220

Likhtman AE, McLeish TCB (2002) Quantitative theory for linear dynamics of linear entangled polymers. Macromolecules 35:6332–6343

Luap C, Müller C, Schweizer T, Venerus DC (2005) Simultaneous stress and birefringence measurements during uniaxial elongation of polystyrene melts with narrow molecular weight distribution. Rheol Acta 45:83–91

Luap C, Karlina M, Schweizer T, Venerus DC (2006) Limit of validity of the stress-optical rule for polystyrene melts: influence of polydispersity. J Non-Newton Fluid Mech 138: 197–203

McHugh AJ, Mackay ME, Khomami B (1987) Measurement of birefringence by the method of isoclinics. J Rheol 31:619–634

Meissner J, Hostettler J (1994) A new elongational rheometer for polymer melts and other highly viscoelastic liquids. Rheol Acta 33:1–21

Meissner J, Garbella RW, Hostettler J (1989) Measuring normal stress differences in polymer melt shear flow. J Rheol 33:843–864

Öttinger HC (1999) Letter to the editor: end effects in flow-birefringence experiments for polymer melts. J Rheol 43:253–259

Peters GWM, Schoonen JFM, Baaijens FPT, Meijer HEH (1999) On the performance of enhanced constitutive models for polymer melts in a cross-slot flow. J Non-Newton Fluid Mech 82:387–427

Pollett WFO (1995) Rheological behaviour of continuously sheared polythene. Br J Appl Phys 6:199–206

Rajagopalan D, Armstrong RA, Brown RA (1990) Calculation of steady viscoelastic flow using a multimode Maxwell model—application of the explicitly elliptic momentum equation [EEME] formulation. J Non-Newton Fluid Mech 36:135–157

Rajagopalan D, Byars JA, Armstrong RC, Brown RA, Lee JS, Fuller GG (1992) Comparison of numerical simulations and birefringence measurements in viscoelastic flow between eccentric rotating cylinders. J Rheol 36:1349–1375

Schoonen JFM, Swartjes FHM, Peters GWM, Baaijens FPT, Meijer HEH (1998) A 3D numerical/experimental study on a stagnation flow of a polyisobutylene solution. J Non-Newton Fluid Mech 79:529–561

Schweizer T (2000) The uniaxial elongational rheometer RME—six years of experience. Rheol Acta 39:428–443

Schweizer T (2002) Measurement of the first and second normal stress differences in a polystyrene melt with a cone and partitioned plate tool. Rheol Acta 41:337–344

Schweizer T (2003) Comparing cone-partitioned plate and cone-standard plate shear rheometry of a polystyrene melt. J Rheol 47:1071–1085

Soulages J (2007) Flow birefringence and velocity measurements for polymer melts in a cross-slot flow channel. PhD thesis, ETH Zurich

Soulages J, Schweizer T, Venerus DC, Hostettler J, Mettler F, Kröger M, Öttinger HC (2007) Lubricated optical rheometer for the study of two-dimensional complex flows of polymer melts. J Non-Newton Fluid Mech 150:43–55

Talwar KK, Khomami B (1992) Applications of higher order finite element methods to viscoelastic flow in porous media. J Rheol 36:1377–1416

Talwar KK, Khomami B (1995) Higher order finite element techniques for viscoelastic flow problems with change of type. J Non-Newton Fluid Mech 59:49–72

Talwar KK, Ganpule HK, Khomami B (1994) A note on selection of spaces in computation of viscoelastic flows using the hp-finite element method. J Non-Newton Fluid Mech 52:293–307

Tzoumanekas C, Theodorou DN (2006) From atomistic simulations to slip-link models of entangled polymer melts: hierarchical strategies for the prediction of rheological properties. Curr Opin Solid State Mater Sci 10:61–72

Venerus DC, Zhu SH, Öttinger HC (1999) Stress and birefringence measurements during the uniaxial elongation of polystyrene melts. J Rheol 43:795–813

Verbeeten WMH, Peters GWM, Baaijens FPT (2002) Viscoelastic analysis of complex polymer melt flows using the eXtended Pom-Pom model. J Non-Newton Fluid Mech 108:301–326

Vladkov M, Barrat JL (2006) Linear and nonlinear viscoelasticity of a model unentangled polymer melt: molecular dynamics and Rouse modes analysis. Macromol Theory Simul 15: 252–262

Wagner MH, Bastian H, Hachmann P, Meissner J, Kurzbeck S, Münstedt H, Langouche F (2000) The strain-hardening behaviour of linear and long-chain-branched polyolefin melts in extensional flows. Rheol Acta 39:97–109

Wales JLS (1976) The application of flow birefringence to rheological studies of polymer melts. PhD thesis, Delft University of Technology

Winter HH, Mours M (1990–2004) Innovative rheological interface software, version 8.0. IRIS Development, Amherst, MA